TMS 2017

146th Annual Meeting & Exhibition

SUPPLEMENTAL PROCEEDINGS

TMS

Springer

The Minerals, Metals & Materials Series

The TMS 2017 Annual Meeting Supplemental Proceedings is a collection of papers from the TMS 2017 Annual Meeting & Exhibition, held February 26–March 2 in San Diego, California, USA. The papers in this volume represent 21 symposia from the meeting. This volume, along with the other proceedings volumes published for the meeting, and archival journals, such as *Metallurgical and Materials Transactions* and *Journal of Electronic Materials*, represents the available written record of the 80 symposia held at TMS 2017.

The Minerals, Metals & Materials Society
Editor

TMS 2017
146th Annual Meeting & Exhibition Supplemental Proceedings

TMS

Springer

Editor
The Minerals, Metals & Materials Society
Pittsburgh, PA
USA

ISSN 2367-1181 ISSN 2367-1696 (electronic)
The Minerals, Metals & Materials Series
ISBN 978-3-319-51492-5 ISBN 978-3-319-51493-2 (eBook)
DOI 10.1007/978-3-319-51493-2
TMS owns copyright; Springer has full publishing rights

Library of Congress Control Number: 2016960778

Printed on acid-free paper

This Springer imprint is published by Springer Nature
The registered company is Springer International Publishing AG
The registered company address is: Gewerbestrasse 11, 6330 Cham, Switzerland

Contents

Part I 2017 Symposium on Functional Nanomaterials: Emerging Nanomaterials and Nanotechnology

High-Performance Supercapacitors Based on Hierarchical VOx Microspheres Forming from Hyperbranched Nanoribbons 3
Chuang Wei, Hong-Yi Li, Zhao Yang and Bing Xie

Potential of Magnetotactic Bacteria for the Fabrication of Iron Nanoparticles 13
T. Thuy Minh Nguyen, Manish D. Baviskar and Paul Bernazzani

Facile Green Synthesis and Characterization of Water Soluble Superparamagnetic Iron Oxide-Gold Porphyrin Conjugate for Improved Photodynamic Therapy 23
Olayemi J. Fakayode, Sandile P. Songca and Oluwatobi S. Oluwafemi

Synthesis of AgNP's from Industrial Waste Using Electrochemical Techniques 29
J. A. Elizalde Mata, R. F. Islas Hernández, J. L. Navarro Jiménez, P. A. Ramírez Ortega, M. U. Flores Guerrero and L. García Hernández

Synthesis of Mn_2O_3 Nanopowders with Urea and Citric Acid by Solution Combustion Route 39
Esma Yilmaz, M. Seref Sonmez, Bora Derin, Filiz Cinar Sahin and Onuralp Yucel

Part II Additive Manufacturing of Metals: Establishing Location-Specific Processing-Microstructure-Property Relationships

Evolution of Aluminum Alloys Structure at Production Phases of 3D Products by Methods of Additive Technologies 49
Victor Mann, Aleksandr Krokhin, Aleksandr Alabin, Sergey Zmanovskiy, Valentin Konkevich and Ivan Redkin

Characterization of Multiperforated Plates Manufactured by SLM and EBM for Aeroengine Applications 61
M. Thomas, O. Lambert, C. Davoine, F. Popoff, C. Dupuy, P. Peyre and R. Dendievel

Direct Laser Metal Deposition of Eutectic Al-Si Alloy for Automotive Applications 71
Amrinder Singh, Abhishek Ramakrishnan and Guru Prasad Dinda

Additive Manufacturing to Produce Standard and Custom Alloy Titanium 81
James C. Withers and Sion M. Pickard

Aiming for Modeling-Assisted Tailored Designs for Additive Manufacturing 91
Dayalan R. Gunasegaram, Anthony B. Murphy, Sharen J. Cummins, Vincent Lemiale, Gary W. Delaney, Vu Nguyen and Yuqing Feng

Part III Additive Manufacturing: Building the Pathway towards Process and Material Qualification

The Use of Laser Ultrasound to Detect Defects in Laser Melted Parts 105
Sarah Everton, Phill Dickens, Chris Tuck, Ben Dutton and David Wimpenny

SLM (Near)-Net-Shape Part Design Optimization Based on Numerical Prediction of Process Induced Distortions 117
Maria San Sebastian, Iñaki Setien, Ane Miren Mancisidor and Alberto Echeverria

Optimizing, Fabricating and Characterizing Additively Manufactured Heat Exchanger Tubing 127
Paul Korinko, John Bobbitt, Haley McKee, Frederick List and S. S. Babu

Scaling Relationships for Direct Ink Writing with Acoustic Focusing 137
Leanne Friedrich, Rachel Collino, Tyler Ray and Matthew Begley

The Influence of Gas Cooling in Context of Wire Arc Additive Manufacturing—A Novel Strategy of Affecting Grain Structure and Size 147
Philipp Henckell, Karsten Günther, Yarop Ali, Jean Pierre Bergmann, Jürgen Scholz and Pierre Forêt

Microstructure and Mechanical Properties of Laser Deposited Ni/WC Metal Matrix Composite Coatings 157
Abhishek Ramakrishnan, Amrinder Singh and Guru Prasad Dinda

Composite Powder Consolidation Using Selective Laser Melting: Input Energy/Porosity Morphology/Balling Effect Relation 169
H. Salem, H. G. Salem and M. M. Attallah

Part IV Advanced Characterization Techniques for Quantifying and Modeling Deformation Mechanisms

Strain Localization Structures in Textured Magnesium AZ31 Under Reversed Loading via Microscopic Digital Image Correlation 183
Enver Kapan, Nima Shafaghi, Sevinç Uçar and C. Can Aydıner

Deformation and Strengthening Mechanisms in AISI 321 Austenitic Stainless Steel Under Both Dynamic and Quasi-Static Loading Conditions 191
A. A. Tiamiyu, A. G. Odeshi and J. A. Szpunar

Analysis of Dislocation Structures in Ferritic and Dual Phase Steels Regarding Continuous and Discontinuous Loading Paths 203
Gregory Gerstein, Till Clausmeyer, Florian Gutknecht, A. Erman Tekkaya and Florian Nürnberger

Microstructural Characterization of Inconel 600 Tubes After Tensile Tests at Various Temperatures and Strain Rates 211
Cécile Davoine, Vincent Marcadon, David Lévêque, Fabienne Popoff, Nicolas Horezan, Denis Boivin and Gérald Portemont

Part V Advanced High-Strength Steels

Influences of Thermomechanical Treatments on the Microcstructure Evolution and Mechanical Properties of Nano-precipitates Strengthened Steels 221
Yu Zhao, Songsong Xu, Hao Guo, Junpeng Li and Z. W. Zhang

Effects of Solid Solution Treatment on the Microstructure and Mechanical Properties in the Ultra-High Strength Steel Strengthened by Nanoscale Particles 233
Songsong Xu, Yu Zhao, Hao Guo, Mingxing Qiu, Jing Zhang, Junpeng Li and Zhongwu Zhang

Effects of Microstructure on the Strain Rate Sensitivity of Advanced Steels 243
Rakan Alturk, Steven Mates, Zeren Xu and Fadi Abu-Farha

Part VI Advanced Materials in Dental and Orthopedic Applications

Characterization of Chitin Synthesized from Snail Shell 257
S. O. Adeosun, O. P. Gbenebor, E. I. Akpan and S. A. Olaleye

Titanium-Magnesium Composite for Dental Implants (BIACOM) 271
Martin Balog, Mateja Snajdar, Peter Krizik, Zdravko Schauperl, Zlatko Stanec and Amir Catic

Part VII Alloys and Compounds for Thermoelectric and Solar Cell Applications V

Thermoelectric Behaviour of Polyvinyl Acetate/CNT Composites 287
Hussein Badr, Mostafa Amr Youssef, Hebatullah Sayed Abd Elsalam, Mirna Abd Elrahman Mohamed, Mohamed Gamal El-kholy, Iman S. El-Mahallawi and Ahmed A. Abdel-Rehim

Part VIII Applications of Solidification Fundamentals

Microstructure Characteristics of A356 Nanocomposites Manufactured via Ultrasonic Cavitation Processing Under Controlled Solidification Conditions 297
Yang Xuan and Laurentiu Nastac

Part IX Biological Materials Science

Development of Sponge Structure and Casting Conditions for Absorbable Magnesium Bone Implants 307
Stefan Julmi, Christian Klose, Ann-Kathrin Krüger, Peter Wriggers and Hans Jürgen Maier

Osteoporosis and Fatigue Fracture Prevention by Analysis of Bone Microdamage 319
Gerardo Presbítero, David Gutiérrez and David Taylor

Bone Remodeling Under Tooth Loading 331
Kangning Su, Li Yuan and Jing Du

Investigating Biochemical Constituents of *Cymbopogon citratus* Leaf: Prospects on Total Corrosion of Concrete Steel-Reinforcement in Acidic-Sulphate Medium 341
Joshua Olusegun Okeniyi, Elizabeth Toyin Okeniyi, Olubanke Olujoke Ogunlana, Taiwo Felicia Owoeye and Oluseyi Ebenezer Ogunlana

Two-Step Sintering Effects on the Microstructure and Mechanical Properties of Forsterite Scaffolds 353
Fariborz Tavangarian, Lindsay Childs, Guoqiang Li, Dakota Wooten and Bryant Cornwell

Part X Bulk Metallic Glasses XIV

Material Behavior in Micro Milling of Zirconium Based Bulk Metallic Glass 363
Boyuan Xie, Maroju N. Kumar, David P. Yan and Xiaoliang Jin

Part XI Computational Thermodynamics and Kinetics

Comparison of the Phase-Field Models to Predict the Recrystallization Kinetics 377
Julia Kundin

RETRACTED CHAPTER: Surface Reaction and Transport in Oxides Formed on FeCrAl Alloys in High Temperature Nitridation Environments 387
Christine Geers, Vedad Babic, Lars-Gunnar Johansson and Itai Panas

Atomic-Scale Modeling of Fe-Al-Mn-C Alloy Using Pair Models and Monte-Carlo Calculations 393
Jérôme Dequeker, Alexandre Legris, Rémy Besson and Ludovic Thuinet

Control Technique Study of Non-metallic Inclusions in Low Carbon Steel by Rare Earth Final Deoxidization 403
Bowen Peng, Fangjie Li, Shaobo Zheng and Huigai Li

Effect of Cooling Rate on Phase Transformation and Microstructure Evolution in a Large Size Forged Ingot of Medium Carbon Low Alloy Steel 413
Emna Ben Fredj, Hadi Ghasemi Nanesa, Davood Shahriari, Jean-Benoit Morin and Mohammad Jahazi

Formation and Control of CaS Inclusion in Gear Steel 20MnCr5 425
Jie Xu, Jianxun Fu, Yanxin Wu and Xu Li

Investigations on the Mechanical Deformation of Amorphous Alloy Nanowires Using Phase-Field Modeling and Thermodynamics Avalanche Models 435
Guangping Zheng

Thermodynamic Modeling of Al-Fe-Cr Ternary System 443
Shusen Wang, Zhu Li, Ziwei Qin, Shihua Wang, Xionggang Lu and Chonghe Li

Part XII Defects and Properties of Cast Metals

A Modeling and Experimental Investigation on the Formation of Acicular Silicon and Sludge in High Pressure Die Casting of a Modified A383 Alloy 457
Mikko Kärkkäinen, Tao Liu, Laurentiu Nastac, Luke Brewer, Vishweshwar Arvikar and Ilya Levin

Hot-Tearing of Multicomponent Al-Cu Alloys Based on Casting Load Measurements in a Constrained Permanent Mold 465
Adrian S. Sabau, Seyed Mirmiran, Christopher Glaspie, Shimin Li, Diran Apelian, Amit Shyam, J. Allen Haynes and Andres F. Rodriguez

Effect of Molybdenum Content, Pouring Temperature and Cooling Rate on the Casting Defects of High Chromium White Cast Iron 475
Izudin Dugic

Effect of Various Aluminum Content on the Formation of Inclusion 483
Yan Luo, Lifeng Zhang, Wen Yang and Ping Shen

Effect of Segregated Alloying Elements on the High Strength Steel Properties: Application to the Large Size Ingot Casting Simulation 491
Chunping Zhang, Davood Shahriari, Abdelhalim Loucif, Mohammad Jahazi, Louis-Philippe Lapierre-Boire and Rami Tremblay

Thermal-Mechanical Model of Depression Formation in Steel Continuous Casting 501
Matthew L.S. Zappulla and Brian G. Thomas

Study for the Initiation Locations of Longitudinal Surface Cracks on Beam Blank in the Mould of Continuous Casting 511
Wei Chen, Xingwang Yu, Ying Chen and Baoxiang Wang

The Influence of SEN and Upper Nozzle Design on the Flow Character for the Slab Quality 521
Yu Yanwen

Effect of the Addition of Ce and Si on Hot Cracking Behavior of SiMn Alloy During the Solidification Process 529
Zhiqiang Zhou, Zizong Zhu, Yuchuan Ding and Shengnan Zhou

Modeling and Predication of Shrinkage Porosity Formation in Steel Ingot 539
Chaojie Zhang, Yanping Bao, Min Wang and Lechen Zhang

Numerical Analysis of Coupled Turbulent Flow and Macroscopic Solidification in a Billet Continuous Casting Mould with Electromagnetic Stirring 551
H. An, Yanping Bao, M. Wang and L. Zhao

Part XIII Environmentally Assisted Cracking: Theory and Practice

Hydrogen Embrittlement and Hydrogen-Enhanced Strain-Induced Vacancies in α-Iron 571
Y. Matsumoto, N. Kurihara, H. Suzuki and K. Takai

Factors Causing Hydrogen Embrittlement of Cold-Drawn Pearlitic Steel Fractured Under Elastic/Plastic Region 579
R. Konno, T. Manabe, N. Matsui, D. Hirakami and K. Takai

Corrosion of Nickel-Titanium, C110, and Al6061 in Gallium-Based Liquid Metal Alloys 587
Jacob Mingear and Darren Hartl

Part XIV General Poster Session

Synthesis and Characterization of Al–B_4C Powders by Mechanical Alloying 599
Hao Guo, Zhongwu Zhang, Yu Zhao, Songsong Xu, Junpeng Li and Jing Zhang

Direct Conversion of Celestite to $SrCO_3$ by Wet Milling 609
Raşit Sezer, Ayşegül Bilen, İbrahim Göksel Hizli, Selim Ertürk and Cüneyt Arslan

Part XV High Temperature Electrochemistry III

Electrochemistry in Molten LiF-BeF_2 Salt for Fluoride Salt-Cooled High Temperature Reactor Applications 617
W. H. Doniger, T. Chrobak, B. Kelleher, K. Dolan, G. Cao, M. Anderson and K. Sridharan

Impurity Removal from Titanium Oxycarbide 629
Farzin Fatollahi-Fard and Petrus Christiaan Pistorius

New Generation Molten Oxide Energy Materials R&D 637
Valery V. Belousov

Effects of Oxide Precursor Preparation Parameters on the Electrochemical Reduction of Tantalum Pentoxide in Calcium Chloride Melt 651
Maureen P. Chorney, Bridger P. Hurley, Prabhat K. Tripathy and Jerome P. Downey

The Effect of Temperature on Electrochemical Codeposition of Mg–Ni Hydrogen Storage Alloys from Molten Salt System 657
Gökçe Hapçı Ağaoğlu and Gökhan Orhan

Part XVI Materials and Fuels for the Current and Advanced Nuclear Reactors VI

Diffusion Studies in the Development of an FCCI Barrier for High-Burnup Metallic Nuclear Fuel 667
Daniel Eichel and James Vollmer

Part XVII Materials Engineering of Soft Magnets for Power and Energy Applications

Development of Mold Inductor for Power Conversion System 677
Hyungsuk Kim, Yeon Jun Chung, Seung Nam Yang and Tae Kyung Lee

Effect of Annealing Time on the Texture of a 2.8% Si Non-Oriented Electrical Steel After Inclined and Skew Rolling 683
Mehdi Mehdi, Youliang He, Erik J. Hilinski and Afsaneh Edrisy

Multi-Parameter Magnetic Material Characterization for High Power Medium Frequency Converters 693
Richard Beddingfield and Subhashish Bhattacharya

Part XVIII Phase Transformations and Microstructural Evolution

An Experimental Assessment of the α + α' Miscibility Gap in Fe-Cr 711
Alexander Dahlström, Frederic Danoix, Peter Hedström, Joakim Odqvist and Helena Zapolsky

Phase Transformation, Microstructural Evolution and Property Modification in Rapidly Solidified Grey Cast Iron 719
Olamilekan Oloyede, Robert F. Cochrane and Andrew M. Mullis

Morphology of Order-Disorder Structures in Rapidly Solidified L12 Intermetallics 729
Nafisul Haque, Robert F. Cochrane and Andrew M. Mullis

Part XIX Recent Developments in Biological, Structural and Functional Thin Films and Coatings

Development of Enamel Coatings in Accordance with Recent Regulations of Food Contact Materials 739
Meltem Ipekci, Kagan Benzesik, Filiz Cinar Sahin and Onuralp Yucel

Transmission Probability of Diffusing Particles—A Case Study 747
Kinnari Shah and Nuggehalli M. Ravindra

Preparation of Porous Titanium Oxide Film by Sol-Gel Method 759
Guobo Yang, Baoqiang Xu, Xianjun Lei, Hongpin Dai, Xutao Guo, Jian Wu and Bin Yang

Part XX Solid State Precipitation

Hydride Precipitates in Zirconium Alloys: Evolution of Dissolution and Precipitation Temperatures During Thermal Cycling Correlated to Microstructure Features 771
Egle Conforto, Stephane Cohendoz, Patrick Girault, Cyril Berziou and Xavier Feaugas

Analysis of β´ Cu_4Ti Precipitation in Cu-Ti Alloys by Conventional and Diffusion-Couple Methods 783
Felipe Hernandez-Santiago, Victor M. Lopez-Hirata, Pamela E. Hernandez-Duran, Maribel L. Saucedo-Muñoz and Erika O. Avila-Davila

Carbide Precipitation in a Low Alloy Ferritic Steel 791
M. L. Saucedo-Muñoz, R. Gómez-Martínez, A. Ortiz-Mariscal, V. M. Lopez-Hirata, J. D. Villegas-Cardenas and J. L. Gonzalez-Velazquez

Part XXI Student-Run Symposium: Building Bridges—Connecting Academic and Industry Research

Fundamental Principles for a Successful Collaboration Between University and Metalworking Industries 803
Silvia Lombardo, Federico Gobber and Mario Rosso

Retraction Note to: Surface Reaction and Transport in Oxides Formed on FeCrAl Alloys in High Temperature Nitridation Environments E1
Christine Geers, Vedad Babic, Lars-Gunnar Johansson and Itai Panas

Author Index 811

Subject Index 815

Part I
2017 Symposium on Functional Nanomaterials: Emerging Nanomaterials and Nanotechnology

High-Performance Supercapacitors Based on Hierarchical VOx Microspheres Forming from Hyperbranched Nanoribbons

Chuang Wei, Hong-Yi Li, Zhao Yang and Bing Xie

Abstract Novel VOx nanomaterials as high performance electrode materials of supercapacitors were successfully synthesized by solvothermal method using V_2O_5, H_2O_2, $(NH_4)_2SO_4$ and EG (Ethylene Glycol). These as-prepared nanomaterials are hierarchical microspheres with diameter of ~5 μm, which formed from hyperbranched growth of nanoribbons. According to XRD and TEM, these hierarchical VOx microspheres consist of V_6O_{13} with metallic conductivity and VO_2. These materials exhibited a tremendous specific capacitance of 581 F/g, with corresponding volumetric specific capacitance of 3.94 F/cm^3, at 0.6 A/g in the potential range of 0 to 1.2 V when used as supercapacitor electrodes in a solution of 1 M $LiNO_3$. The energy density is as high as 29 Wh/kg, which is much higher than those of many other symmetrical supercapacitors. In addition, the capacity retention of 65% was achieved even after 2000 cycles, demonstrating high performance of vanadium oxide nanomaterials used in supercapacitors.

Keywords Supercapacitor · VOx · Nanomaterial · Microsphere · Nanoribbons

Introduction

In recent years, supercapacitors have attracted considerable attention due to their energy density higher than conventional capacitors. The supercapacitors are also known for their higher power density and longer cycle life than that of batteries [1–3]. Vanadium oxides, such as V_2O_5, VO_2, and V_2O_3 etc., have been investigated widely as materials for energy storage [4]. The theoretical specific capacitance and potential window of vanadium oxides are relatively high owning to the multiple valance from V(II) to V(V). Furthermore, most of vanadium oxides (except VO_2) are lamellar

C. Wei (✉) · H.-Y. Li (✉) · Z. Yang · B. Xie
College of Materials Science and Engineering, Chongqing University, Chongqing 400044, China
e-mail: hongyi.li@cqu.edu.cn

The Minerals, Metals & Materials Society, *TMS 2017 146th Annual Meeting & Exhibition Supplemental Proceedings*, The Minerals, Metals & Materials Series,
DOI 10.1007/978-3-319-51493-2_1

structure, which contributes to ions insertion/extraction during the charge/discharge process, improving specific capacitance of supercapacitors. Therefore, vanadium oxides are promising materials as electrode materials for supercapacitors.

Vanadium oxide is usually made into nanomaterials to improve electrochemical properties of supercapacitors by increasing the specific surface of electrode materials. For example, 0D nanomaterial of V_2O_5 nanoparticles [5], 1D nanomaterials of V_2O_5 nanowires [6], and 2D nanomaterials VO_2 nanobelts [7] have been synthesized and applied in supercapacitors. However, these low dimensional nanomaterials are more likely to agglomerate severely leading to inferior cycling stability of supercapacitors. So vanadium oxides have been prepared as 3D nanomaterials to avoid this phenomenon, such as starfruit-like VO_2 [8] and V_2O_5 nanosheets based 3D architecture [9]. But the specific capacitances of supercapacitors even based on 3D pure vanadium oxide nanomaterials (200–300 F/g) still cannot approach that of RuO_2 due to the lower electric conductivity of common vanadium oxides.

In this work, 3D mesoporous hierarchical microspheres, composed of VO_2 and uncommon vanadium oxide V_6O_{13} which is metallically conductive [10], have been synthesized. These microspheres also possess high specific surface and high density and thus exhibits a high specific capacitance (581 F/g) and high volumetric energy density (3.94 F/cm^3). The cycling stability of these microspheres is good due to the stable 3D nanostructure of hierarchical VOx microspheres. This work proves a strategy to improve the conductivity and stability of electrode materials, which has potential application in the future.

Experiment

Synthesis of Samples

These hierarchical VOx microspheres were prepared as follows: 4.5 mmol V_2O_5 powder was dissolved in 32.64 mL 10% H_2O_2 solution with vigorously magnetic stirring at 25 °C for 2 h in dark. 6 mL obtained reddish solution was mixed with 15 mL ethylene glycol (EG) and 15 mL de-ionized water (Millipore Aquelix) and 0.396 g $(NH_4)_2SO_4$, then stirred for about 10 min in order to obtain homogeneous solution. After that, the mixture was transferred into a 50 mL Teflon container and sealed in an autoclave, which was placed in a electrical oven and heated at 120 °C for 24 h, which was then cooled down to room temperature in the air. The black precipitates existed in the bottom of Teflon were collected by centrifugation, followed by washed with de-ionized water and anhydrous alcohol for 3 times, respectively. The precipitates were dried in vacuum at 80 °C for 12 h and then calcinated in tube furnace at 350 ° for 3 h in flowing N_2 by heating from room temperature to 350 °C at the rate of 10 °C/min. After cooling down to room temperature in N_2 atmosphere, hierarchical VOx microspheres were finally obtained. All reagents used in the experiments are of analytical grade and used without any further purification.

Characterization

The chemical composition of products was characterized by X-ray diffraction (XRD; Rigaku D/Max 2500 PC, Cu Kα, Japan). The morphology and microstructure of hierarchical VOx microspheres were characterized by field emission scanning electron microscopy (FESEM; FEI Nova 400, Netherland) and transmission electron microscopy (TEM; Zeiss LIBRA 200, Germany). The focused ion beam (FIB) cutting was conducted in Zeiss AURIGA FIB (Germany).

Electrochemical Measurements

CHI660E electrochemical workstation was used to measure the electrochemical performance. The working electrode was prepared by mixing the active materials, acetylene black and polyvinylidene fluoride (PVDF) with a mass ratio of 70:20:10. The mixture then was made into slurry by using 1-methyl-2-pyrrolidinone (NMP) as a solvent. Subsequently, the slurry of mixture was spread on a round foam nickel with a diameter of 1.7 cm and dried under vacuum at 120 °C for 12 h, the working electrode then was obtained, which contained about 3 mg active materials. Two-electrode system with two working electrodes sealed in a button cell and 1 M $LiNO_3$ as the electrolyte was adopted to measure the electrochemical. The two working electrodes with same mass of materials were separated by a polypropylene membrane. The button cell should be kept static for 24 h so that the electrode materials were thoroughly wetted with the electrolyte. The cyclic voltammetry (CV) and galvanostatic charging/discharging (GCD) measurements were conducted on the electrochemical workstation. All the electrochemical tests were performed at room temperature.

Results and Discussion

Chemical components of products were investigated by XRD. Figure 1 shows the typical diffraction patterns of the as-prepared products. It can be seen in the XRD patterns that the apparent peaks at $2\theta = 15.4°$, 25.3°, 49.3° and 59.6° are well indexed to monoclinic VO_2 (JCPDS no. 31-1438) with standard lattice constants of a = 12.03 Å, b = 3.69 Å, c = 6.42 Å ($\alpha = 90.0°$, $\beta = 106.6°$, $\gamma = 90.0°$), while the rest of main peaks are attributed to monoclinic V_6O_{13} (JCPDS no. 43-1050) with standard lattice constants of a = 11.92 Å, b = 3.68 Å, c = 10.14 Å ($\alpha = 90.0°$, $\beta = 100.9°$, $\gamma = 90.0°$). Therefore, XRD patterns indicate that the products are mixture of VO_2 and V_6O_{13} crystals.

The morphology of as-prepared products was shown in Fig. 2. It can be seen from Fig. 2a–b that the products are microspheres with diameter of ~5 μm. These

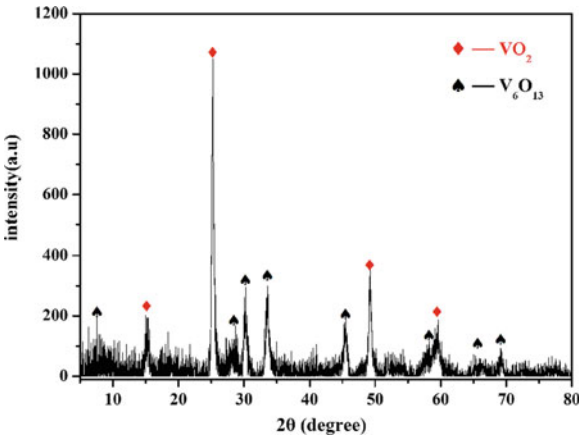

Fig. 1 XRD pattern of the hierarchical VOx microspheres

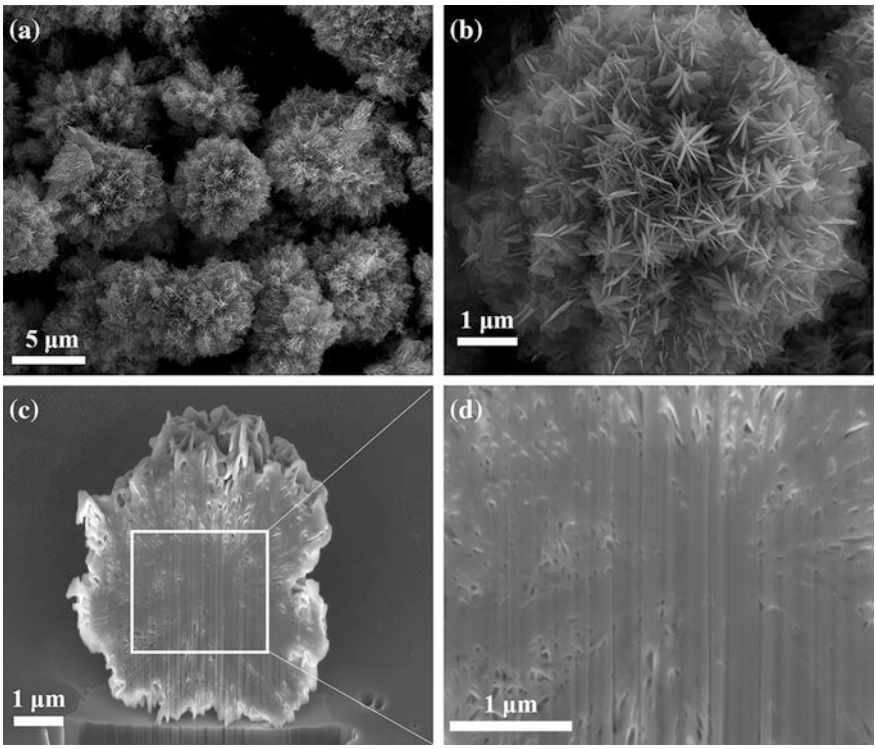

Fig. 2 SEM images of as-prepared products (**a**–**b**) and cross-section of the microsphere cut by FIB (**c**–**d**)

microspheres are made up of ~400 nm long nanoribbons. 4–6 nanoribbons combine together radially, with one end clustering in the centre and the other end dispersing around. To further figure out internal structure of the microsphere, FIB was adopted to cut off a part of microsphere as presented in Fig. 2c–d. It is clear that the interior of microsphere is not completely solid, some radial nanobelts (dark belt-like areas in Fig. 2d) play the roles of backbones, on which the nanoribbons grow. The hyperbranching growth of nanobelts and nanoribbons formed those microspheres. These solid nanobelt backbones contribute to high structure stability of microspheres. The hierarchical structure, resulting from the hyperbranching growth, brings in loads of pores and large surface area, which are beneficial to the easy accessibility of electrolyte ions. It thus indicates the potential high performance of the as-prepared hierarchical microspheres as electrodes of supercapacitors.

To further investigate the microstructure of products, TEM studies were used (Fig. 3). A cluster of hierarchical VOx microspheres was observed in Fig. 3a, as can be seen in the image the deep dark and wide belt-like areas distribute radially and form the backbones of the cluster, which agrees with SEM images in Fig. 2. At the same time, nanoribbons grow around those nanobelts as the light dark areas shown in Fig. 3a. The high resolution TEM images of a part of cluster display the combination of nanobelts and nanoribbons shown in Fig. 3b–c. The deep dark areas are connected to nanobelts and the light dark areas are nanoribbons. The interplanar spacing of 0.27 and 0.32 nm are in agreement with the spacing of V_6O_{13} (310) plane and ($\bar{2}03$) plane, respectively, as indicated in Fig. 2, while the lattice fringes with spacing of 0.16 and 0.19 nm are also found in Fig. 3c, which correspond to the spacing of ($\bar{4}04$) and ($\bar{1}13$) plane, respectively, in VO_2 crystal as shown in XRD. According to TEM images, it further confirms the existence of V_6O_{13} and VO_2.

The electrochemical properties of hierarchical VOx microspheres were investigated as electrodes for supercapacitor using a two-electrode cell configuration. Cyclic voltammetry (CV) and galvanostatic charging/discharging measurements were conducted. Fig 4a exhibits the typical CV curve of hierarchical VOx microspheres at the scan rates of 5 mV/s, 15 mV/s, 20 mV/s, 30 mV/s and

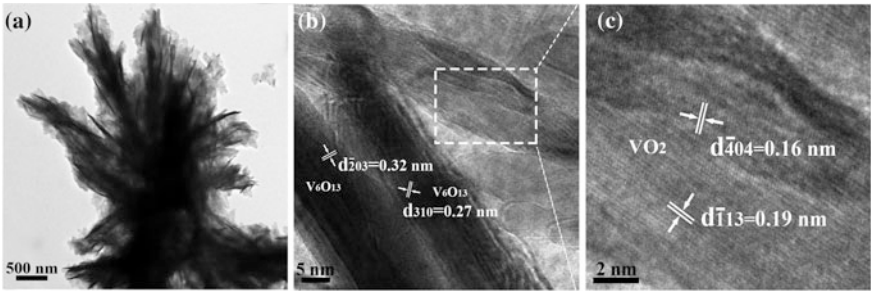

Fig. 3 TEM images of the hierarchical microspheres

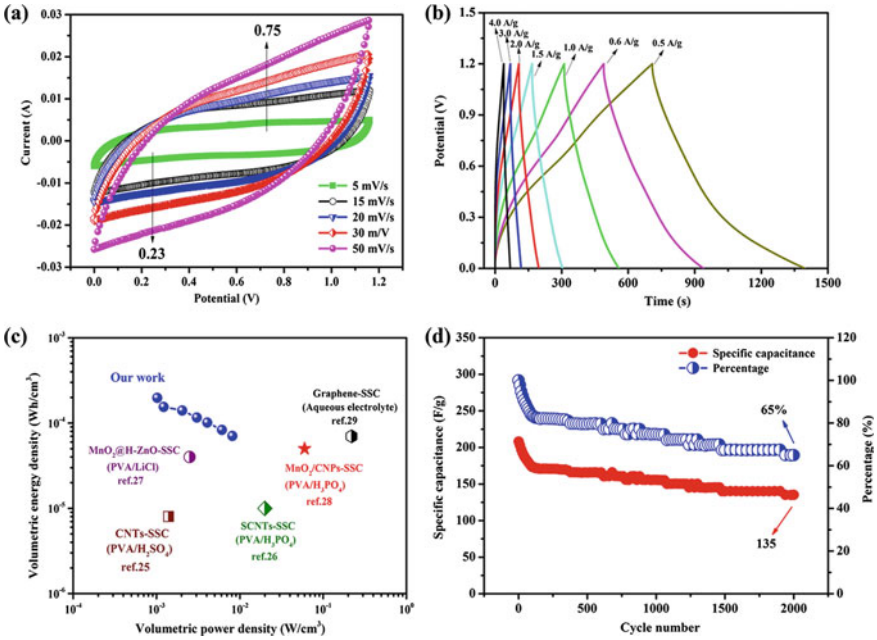

Fig. 4 **a** CV curves of the hierarchical VOx microspheres at different scan rates; **b** Galvanostatic charging/discharging curves of hierarchical VOx microspheres at different current densities; **c** Ragone plot of the symmetric supercapacitor based on hierarchical VOx microspheres; **d** Cycling performance of hierarchical VOx microspheres at current density of 4.0 A/g

50 mV/s, respectively, within the potential range from 0 V to 1.2 V. It is clear that the shape of CV curve at low scan rate is nearly rectangular, following the electric double layer charging/discharging mechanism, which indicates that hierarchical VOx microspheres own perfect charge storage ability and high efficiency. A pair of redox peaks of the CV curves at 5 mV/s advent at 0.23 and 0.75 V, and the electrochemical redox reactions associated with this pair of redox peaks as follows:

$$VO_x + xLi^+ + xe^- \leftrightarrow Li_xVO_x \quad (1)$$

where x is the mole fraction of intercalated Li^+ ions. This pair of redox peaks indicates the charge storage mechanism is pseudocapacitance, which has broad application prospect for electrode materials of supercapacitors [11]. This superior performance of the electrode materials is mainly due to V_6O_{13} crystals with metallic conductivity that contribute to the electron transfer. But at scan rate as high as 50 mV/s, the curve exhibits a deformed shape and the redox peaks are not obvious as low scan rate, the reason is that it is difficult for Li^+ ions to intercalate and deintercalate the mesopores deep inside the microspheres at such high scan rate Fig. 4b shows the galvanostatic charging/discharging curve at different current densities. The specific capacitance of supercapacitors can be calculated through

galvanostatic charging/discharging measurement, the corresponding formula as follows:

$$C = 2I\Delta t/m\Delta V \tag{2}$$

where C is the specific capacitance, I is the constant current; Δt is the discharging time; m is the mass of electrode material; ΔV is the potential drop upon discharging. At the current density of 0.5 A/g (i.e. 0.8 mA/cm^2), the gravimetric specific capacitance of hierarchical VOx microspheres is as remarkably high as 581 F/g, while the corresponding volumetric specific capacitance is 3.94 F/cm^3. In terms of the value of gravimetric specific capacitance, it is much higher than most of reported vanadium oxide nanostructures based electrodes such as flower-like V_2O_3 (218 F/g at 0.05 A/g), VO_2 nanobelts (191 F/g at 1 A/g), V_4O_9 microflowers (392 F/g at 0.5 A/g) and polypyrrole coated V_2O_5 nanoribbons (308 F/g at 0.1 A/g), and even vanadium oxide/carbon composite nanostructures including Ti-doped VO_x/CNT composites (310 F/g at 5 mV/s) and V_2O_3 nanoflakes@C composites (205 F/g at 0.05 A/g) [2, 12–16]. It is also higher than those of other transition metal materials such as MnO_2 nanorods (298 F/g at 5 mV/s) and flower-like $Co_3(PO_4)_2$ (350 F/g at 1 A/g) [17, 18]. For volumetric specific capacitance, which is also significantly higher than many other reported supercapacitors, such as the asymmetric supercapacitor based on hydrogen-treated (denoted as H-) TiO_2@MnO_2 and H-TiO_2@C (0.71 F/cm^3 at 10 mV/s) [19] and the symmetric supercapacitor based on MnO_2@carbon fiber (2.5 F/cm^3 at 0.02 A/cm^3) [20]. The curves at all current densities exhibit symmetric triangular shape even at a high current density of 4.0 A/g, which indicates that the supercapacitor based on hierarchical VOx microspheres is an ideal capacitor that charge can transport quickly [21, 22]. The reasons associated with such superior specific capacitance of supercapacitor based hierarchical VOx microspheres are that hyperbranched growth of nanoribbons leads to high specific area that provide a large amount of active surface sites for redox reaction to take place in, and hierarchical structure exists mass mesopores which can facilitate the intercalation/deintercalation of electrolyte ions so that the rate of redox reactions on the surface can be increased, and the high metallic conductivity of V_6O_{13} accelerates the electron transfer inside the bulk microspheres, which is beneficial to increasing the redox reaction rate. It is also worthy to point out that VOx microspheres possess higher mass density compared with carbonaceous materials, which can decrease the volume of electrodes and lead to higher volumetric specific capacitances [19, 20].

The energy density (E) and power density (P) are shown in Fig. 4c. According to the two-electrode configuration, E and P are calculated by the following formula:

$$E = 1/8CV^2 \tag{3}$$

$$P = E/\Delta t \tag{4}$$

where C is the specific capacitance, V is the cell voltage and Δt is the discharge time. The maximum energy density was calculated to be 29 Wh/kg at the power density of 150 W/kg and the maximal power density is 1.2 kW/kg at 4.0 A/g. This energy density is much higher than those of symmetrical supercapacitors based on V_2O_5/carbon nanotubes (16 Wh/kg at power density of 800 W/kg) [23] and V_2O_5 nanotube spherical clusters (11.6 Wh/kg at 0.1 A/g) [24]. The corresponding volumetric energy density as shown is 0.2 mWh/cm^3, which is also substantially higher than values reported for other supercapacitors, such as the symmetric supercapacitors (SSC) based on multiple walled carbon nanotubes (0.008 mWh/cm^3 at 1.4 mW/cm^3) [25], single walled carbon nanotubes (0.01 mWh/cm^3 at 0.02 W/cm^3) [26], MnO_2@H-ZnO (0.04 mWh/cm^3 at 2.5 mW/cm^3) [27], MnO_2/Carbon nanoparticles (0.05 mWh/cm^3 at 0.06 W/cm^3) [28], and graphene (0.07 mWh/cm^3 at 0.22 W/cm^3) [29]. The high energy density, together with high power density, is due to the high specific surface area of the hierarchical microspheres, the high conductivity and high density of V_6O_{13} in the hierarchical microspheres.

Another important criterion for supercapacitor is cycling performance examined at 4.0 A/g as shown in Fig. 4d. Notably, 65% of initial specific capacitance has been maintained after 2000 cycles, even though the specific capacitance decreases sharply by 18% of initial value in the first 130 cycles, after which it decreased slightly. The reason of decay is that V(V)-bearing vanadates was dissolved into electrolyte during the charging/discharging process, which is common in supercapacitors and lithium-ion batteries based on vanadium oxide materials [16, 30–32]. Though the capacitance reduced by 35% after 2000 cycles, the cycling stability of hierarchical VOx microspheres is obviously higher than that of other morphologies based on pure vanadium oxides without carbon, especially those with high initial specific capacitances [7, 33]. This remarkable stability benefits from the hyperbranched growth of alternative VO_2 crystals and V_6O_{13} crystals in the microspheres.

Conclusions

In summary, hierarchical VOx microspheres forming from hyperbranched growth of growth of have been successfully synthesized by solvothermal method. These as-prepared VOx microspheres with diameter of ~5 μm are made up of ~400 nm long nanoribbons. Both XRD and TEM indicate that the products consist of V_6O_{13} crystal with good metallic conductive and VO_2 crystal. The hierarchical VOx microspheres prepared for electrode materials of supercapacitors exhibit superior electrochemical performance with high specific capacity of 581 F/g (3.94 F/cm^3) and outstanding energy density of 29 Wh/kg (0.2 mWh/cm^3). The cycling stability of hierarchical VOx microspheres is also obviously higher than many other reported materials.

Acknowledgements The authors would like to acknowledge the financial supports by National Natural Science Foundation of China (No. 21105134 and No. 51474041), the Natural Science Foundation Project of CQ CSTC (No. cstc2012jjB50011) and Fundamental Research Funds for the Central Universities of China (No. 106112015CDJZR465505).

References

1. J.R. Miller, A.F. Burke, Electrochemical capacitors: challenges and opportunities for real-world applications. Electrochem. Soc. Interface **17**(1), 53–57 (2008)
2. K.-J. Huang et al., One-step preparation of layered molybdenum disulfide/multi-walled carbon nanotube composites for enhanced performance supercapacitor. Energy **67**, 234–240 (2014)
3. V. Augustyn, P. Simon, B. Dunn, Pseudocapacitive oxide materials for high-rate electrochemical energy storage. Energy Environ. Sci. **7**(5), 1597–1614 (2014)
4. N. Bahlawane, D. Lenoble, Vanadium oxide compounds: structure, properties, and growth from the gas phase. Chem. Vapor. Depos. **20**(7–9), 299–311 (2014)
5. D.P. Nair et al., Effect of surfactants on electrochemical properties of vanadium-pentoxide nanoparticles synthesized via hydrothermal method. J. Nanosci. Nanotechnol. **15**(6), 4392–4397 (2015)
6. N.N. Wang et al., Facile hydrothermal synthesis of ultrahigh-aspect-ratio V2O5 nanowires for high-performance supercapacitors. Curr. Appl. Phys. **15**(4), 493–498 (2015)
7. H.W. Wang et al., One-step strategy to three-dimensional graphene/VO2 nanobelt composite hydrogels for high performance supercapacitors. J. Mater. Chem. A **2**(4), 1165–1173 (2014)
8. J. Shao et al., One-step hydrothermal synthesis of hexangular starfruit-like vanadium oxide for high power aqueous supercapacitors. J. Power Sources **219**, 253–257 (2012)
9. J.X. Zhu et al., Building 3D structures of vanadium pentoxide nanosheets and application as electrodes in supercapacitors. Nano Lett. **13**(11), 5408–5413 (2013)
10. P.D. Dernier, Structural investigation of the metal-insulator transition in V_6O_{13}. Mater. Res. Bull. **9**(7), 955–963 (1974)
11. M.H. Yu et al., Valence-optimized vanadium oxide supercapacitor electrodes exhibit ultrahigh capacitance and super-long cyclic durability of 100 000 cycles. Adv. Funct. Mater. **25**(23), 3534–3540 (2015)
12. P.H. Jampani et al., High energy density titanium doped-vanadium oxide-vertically aligned CNT composite electrodes for supercapacitor applications. J. Mater. Chem. A **3**(16), 8413–8432 (2015)
13. H. Wang et al., One-step strategy to three-dimensional graphene/VO_2 nanobelt composite hydrogels for high performance supercapacitors. J. Mater. Chem. A **2**(4), 1165–1173 (2014)
14. H. Pang et al., 2D single-or double-layered vanadium oxide nanosheet assembled 3D microflowers: controlled synthesis, growth mechanism, and applications. Nanoscale **5**(17), 7790–7794 (2013)
15. Q. Qu et al., Core–shell structure of polypyrrole grown on V_2O_5 nanoribbon as high performance anode material for supercapacitors. Adv. Energy Mater. **2**(8), 950–955 (2012)
16. H. Liu et al., Flowerlike vanadium sesquioxide: solvothermal preparation and electrochemical properties. ChemPhysChem **11**(15), 3273–3280 (2010)
17. Z.K. Ghouri et al., High-efficiency super capacitors based on hetero-structured alpha-MnO2 nanorods. J. Alloy. Compd. **642**, 210–215 (2015)
18. H.Y. Li et al., Self-assembled 3D cobalt phosphate octahydrate architecture for supercapacitor electrodes. Mater. Lett. **152**, 25–28 (2015)
19. X.H. Lu et al., H-TiO_2@MnO_2//H-TiO_2@C Core-shell nanowires for high performance and flexible asymmetric supercapacitors. Adv. Mater. **25**(2), 267–272 (2013)

20. X. Xiao et al., Fiber-based all-solid-state flexible supercapacitors for self-powered systems. ACS Nano **6**(10), 9200–9206 (2012)
21. M. Kim, J. Kim, Development of high power and energy density microsphere silicon carbide-MnO_2 nanoneedles and thermally oxidized activated carbon asymmetric electrochemical supercapacitors. Phys. Chem. Chem. Phys. **16**(23), 11323–11336 (2014)
22. Y. Hou et al., Nanoporous metal based flexible asymmetric pseudocapacitors. J. Mater. Chem. A **2**(28), 10910–10916 (2014)
23. I. Shakir et al., Ultra-thin and uniform coating of vanadium oxide on multiwall carbon nanotubes through solution based approach for high-performance electrochemical supercapacitors. Electrochim. Acta **111**, 400–404 (2013)
24. S.D. Perera et al., Vanadium oxide nanotube spherical clusters prepared on carbon fabrics for energy storage applications. ACS Appl. Mater. Interfaces **3**(11), 4512–4517 (2011)
25. Y.J. Kang, et al., All-solid-state flexible supercapacitors based on papers coated with carbon nanotubes and ionic-liquid-based gel electrolytes, *Nanotechnology*, **23**(28) (2012). (vol 23, 065401, 2012)
26. M. Kaempgen et al., Printable thin film supercapacitors using single-walled carbon nanotubes. Nano Lett. **9**(5), 1872–1876 (2009)
27. P.H. Yang et al., Hydrogenated ZnO core-shell nanocables for flexible supercapacitors and self-powered systems. ACS Nano **7**(3), 2617–2626 (2013)
28. L.Y. Yuan et al., Flexible solid-state supercapacitors based on carbon nanoparticles/mno_2 nanorods hybrid structure. ACS Nano **6**(1), 656–661 (2012)
29. M.F. El-Kady et al., Laser scribing of high-performance and flexible graphene-based electrochemical capacitors. Science **335**(6074), 1326–1330 (2012)
30. L.J. Cao et al., Ultrathin single-crystalline vanadium pentoxide nanoribbon constructed 3D networks for superior energy storage. J. Mater. Chem. A **2**(32), 13136–13142 (2014)
31. M.-H. Bai et al., Electrodeposition of vanadium oxide-polyaniline composite nanowire electrodes for high energy density supercapacitors. J. Mater. Chem. A **2**(28), 10882–10888 (2014)
32. S.-Z. Huang et al., Annealed vanadium oxide nanowires and nanotubes as high performance cathode materials for lithium ion batteries. J. Mater. Chem. A **2**(34), 14099–14108 (2014)
33. H. Liu, et al., *Chem. Phys. Chem.* **11** (2010)

Potential of Magnetotactic Bacteria for the Fabrication of Iron Nanoparticles

T. Thuy Minh Nguyen, Manish D. Baviskar and Paul Bernazzani

Abstract Magnetotactic bacteria are typically found in soils rich in iron. These prokaryote bacteria have the property of using ingesting atoms of iron and generating magnetosomes of nanoparticles of either diamagnetic or paramagnetic nature within each cell. We report on the use of magnetotatic bacteria for the production of uniform nanoparticles of iron mineral magnetite (Fe_3O_4). The potential for mass production was investigated along with the molecular, physical, and magnetic properties of the magnetosomes using various growth and microscopy techniques. Results reveal that the magnetic particles are stable and that bacteria growth can be optimized to produce magnetosomes with different magnetic properties, suggesting that the industrial development of these bio manufactures lies in the foreseeable future.

Keywords Magnetosomes · Magnetic bacteria · Nanoparticles · Iron

Introduction

The synthetic production of nanoparticles, the cornerstone of nanotechnology, involves various physical and chemical methods. However, a disadvantage of these methods is the production of toxic byproducts, possibly making them not environmentally safe methods [1]. Nanoparticle synthesis using biological systems would follow green chemistry principles as the reagents are eco-friendly including the reducing agent and the capping agent in the reaction [2, 3].

Biogenic nanoparticles involve natural phenomena that take place in the biological systems. Bacteria are considered as the most potent eco-friendly nanofactories [1]. Magnetotactic bacteria (MTB) are a heterogenous group of aquatic microorganisms that have the ability to orient and migrate along geomagnetic field

T. Thuy Minh Nguyen (✉) · M.D. Baviskar · P. Bernazzani
Department of Chemistry and Biochemistry, Lamar University,
Beaumont, TX 77710, USA
e-mail: ttnguyen15@lamar.edu

The Minerals, Metals & Materials Society, *TMS 2017 146th Annual Meeting & Exhibition Supplemental Proceedings*, The Minerals, Metals & Materials Series,
DOI 10.1007/978-3-319-51493-2_2

lines, a behavior named magnetotaxis. This property is based on specific intracellular structures, the magnetosomes which, in most MTB are nanometer-sized, membrane bound magnetic particles, composed of the iron mineral magnetite (Fe_3O_4) or more rarely, greigite (Fe_3S_4). These magnetosomes are organized in one or more straight chains parallel to the long axis of the cells. Such an arrangement confers a magnetic moment to the cell. In the northern hemisphere these MTB are known to move towards the geographic North Pole, while in the southern hemisphere they are known to migrate towards the geographic south. Magnetotactic bacteria are found in diverse aquatic habitats and include coccoid to ovoid cells, rods, vibrios and spirilla from different water bodies (freshwater, seawater), sediment and soil. Reports of South-seeking magnetotactic bacteria found in Southern hemispheres sediments as well as of samples held in similar magnetic conditions in the Northern Hemisphere which verifies the hypothesis that downward direction is advantageous orientation and upward detrimental for the survival of the magneto tactic bacteria with unidirectional motility [4–6].

Bacterial magnetic nanoparticles have great useful potential in biotechnological and biomedical applications. In this study, a liquid growth medium will be modified for cultivation of a magnetotactic bacterium that has been isolated from sediment sample. These modifications include changes in the type and amounts of vitamin, minerals, carbon sources, etc. Serum bottles and designed air-tight laboratory bottles can be used to create microaerobic conditions in order to develop a method for scale-up experiment.

Magnetotactic bacteria (MTB) synthesize unique nanoparticle structures within magnetosomes. MTB's nanoparticles are coated with a thin organic membrane that results in high and homogeneous dispersions in aqueous solutions compared to artificial magnetic nanoparticles, making them ideal biotechnological materials [7, 8]. It has already been demonstrated, that isolation and axenic cultivation of MTB in pure culture is very difficult. To date only a small number of isolates and an even smaller number of genera and species are available [9, 10]. Recently, pure cultivation of magnetic bacteria in defined medium has provided effective advancement on the application of MTB's nanoparticles. Because of MTB's fastidious culture requirements, growth of most of them on a large scale is extremely difficult. Mass cultivation of MTB for magnetosome production may be one of the most important biotechnological processes in the application of MTB's nanoparticles. We report the investigation of a new approach for large-scale production of magnetotactic bacteria. The main goal of this study was development a method with low temperature, lower energy cost and high yield that may make biogenical magnetic nanoparticles a more economical and energy sustainable process than some of the competing processes.

Methodology

Isolation and Screening of Bacteria

Samples were collected in sterile flasks and plastic containers for bacteriological analysis. The samples were stored in dark cold room at 40 °C for 28 days. The magnetotactic (MTB) bacteria were isolated using the race track method. Isolated bacteria were tested for magnetic particle synthesis ability.

Optimization and Validation of Growth Condition

Optimum growth condition and media for each isolates will be optimized by adjusting pH, temperature and Different chemical concentration and oxygen requirement. 250 ml Erlenmeyer flask will be used where 10 ml of Sterile Luria-Bertani (LB) broth liquid media will be used as baseline growth media to identify mixo-tropic growth of magnetic tactic bacteria. Then it will be incubated in Shaker overnight at 30 °C AT 150 RPM. Optical density of culture will be checked after 8 to 10 h at 600 nm using spectrophotometer to determine growth of bacteria.

Optimization of Nano Magnetic Practical Synthesis Process

Isolated cells were seeded in optimized media incubated at optimum growth condition by period analysis of magnet in different growth condition. Prussian blue assay was used to evaluate the presence of magnetosomes.

Source of Microorganism and Liquid Media Preparation

Magnetotactic bacteria were isolated from a water/sediment microcosm that was collected from the Marquez Crater. Control cells acquired from ATCC were also used. After magnetic collection and isolation methods, LB media was used for cultivation experiments. A modified liquid medium (MLM) was also used which contained Wolfe's vitamin solution, Wolfe's mineral solution, sodium succinate, yeast extract, $MgSO_4 \times 7H_2O$, peptone casein, potassium phosphate buffer (pH 7), NH_4Cl, sodium acetate anhydrous, resazurin, ferric citrate, HCl and the pH was adjusted to 7.0. HCl and vitamin solution were added to the MLM after autoclaving.

Microscopy Studies

Microscopy, isolated cells of the MTB were diluted by sterilized phosphate buffer solution (pH = 7, 10 mM) and then cells were placed on the surface of glass slides. The morphology and configuration of the MTB and their magnetosomes were investigated with different staining techniques.

Isolation and Purification of Magnetosomes

The magnetotactic bacteria were harvested by centrifugation (8000 rpm, 15 min, 4 °C) and washed by sterilized phosphate buffer solution (pH = 7.0). Then the precipitated cells were resuspended in 1 N NaOH and boiled for 30 min to lyse the cells. Magnetosomes from the disrupted cells were collected at a graduated cylinder by magnets for 1 h, then the nonmagnetic fluid was removed by aspiration and magnetic nanoparticles washed with buffer. Finally, the magnetosomes attracted to the magnet were carefully suspended in sterilized phosphate buffer solution (pH = 7.0).

Collection of Magnetic bacteria was done based on the cells' swimming response to a magnetic field. The south pole of a permanent magnet was attached outside a jar containing the water and sediment samples, 1 cm above the sediment surface. After 2–4 h 1–2 ml of the water in the bottle near the wall adjoining the magnet was collected with a pipette and transferred to sterile tubes to be used for further studies. "Race track" purification and enrichment of the MTB The modified capillary "race track" (CRT) method was used to purify and enrich the MTB obtained by magnetic collection. A capillary tube (length, 6–9 cm) sealed at one end in a gas flame was filled with medium by means of a long hypodermic syringe and was fitted to the narrow end of a Pasteur pipette. The sample material (magnetically collected cells) was placed on the top of a sterile, wetted cotton plug in the wide mouth end of the pipette that served as a reservoir. The capillary was exposed to a magnetic field produced along it with a permanent magnet for 5 h. The MTB migrated through the cotton plug towards the closed end of the capillary. The tip containing the accumulated MTB was then broken off and with the help of a sterile hypodermic needle the organisms transferred to the sterile enrichment medium taken in test tubes that were incubated at 30–350 °C for about two days. This method was repeated two more times to purify the MTB fully. Isolation of magnetic bacteria. The purified magnetic cells were then isolated by the streak plate method using a magnetic field and preserved (at 40 °C) on the same medium.

Assessment of Culture Magnetism

The isolates were tested for their magnetotactic response using the 'hanging drop technique' under an optical microscope, with the south pole of a bar magnet being placed some 10 cm distant from the slide. Their magnetic response was also tested in terms of the spreading of their growth on the surface of a semisolid (50:50) LB and MSGM medium [0.8% agar]. The isolates were inoculated in a straight line at the center of the medium in petriplates. The plates were incubated in a magnetic field created by placing the opposite poles of two different bar magnets on either side perpendicular to the line of streaking. The growth pattern after incubation was observed for any spreading towards the magnet poles. The isolated magnetic cultures and a known non-magnetic bacterial culture [*E. coli*] as control were grown in the MSGM medium that contained Ferric Quinate as source of iron. After obtaining sufficient growth (approximately 30–40 mg dry weight), the cell mass was separated by centrifugation at 10,000 g in a research centrifuge. The cell mass thus obtained was dried to constant weight at 105 °C in a hot air oven. Iron content of the cell mass was determined by Infra-red and UV-visible spectroscopy on a Model, using the tri-acid digestion method of iron extraction from the cells.

Results and Discussion

Enrichment and Isolation

Magnetotactic bacteria (MTB) were successfully enriched from sediment samples obtained from the Marquez crater using the magnetic collection method and purified by the capillary racetrack method. The mixed bacterial culture that was obtained was observed under a microscope and seen to include more than one morphological type. The streak plate method of isolation as well as a total viable count of the original samples were performed to verify the efficacy of the magnetic purification methods. About four different morphological forms of bacteria were obtained as pure cultures and different individual colony characteristic were observed. The bacteria forms included gram positive rod shaped bacteria, gram negative slender rod and gram positive coccus.

The original samples were grown under different media conditions. Figure 1 present the images of Petrie dishes containing the samples as received and following 10 days of incubation in standard media concentration. The growth potential of the samples is observed and optimization can be obtained. Following culture growth, magnetotactic bacteria were isolated using the race track method. Figure 2 shows the microscopy images of bacteria where two distinctive types were identified, one north seeking magnetotactic bacteria and another south seeking. These findings lead to the assessment of the magnetism and of the capacity of the samples to produce magnetosomes.